École polytechnique fédérale de Lausanne

Semester Project

Master in Computational Science and Engineering

Haemodynamics simulations of abdominal aortic aneurysm: comparisons between pre and post EVAS surgery

Author:
Andrea Scaglioni

Supervisors:
Dr. Claudia Colciago
Prof. Alfio Quarteroni

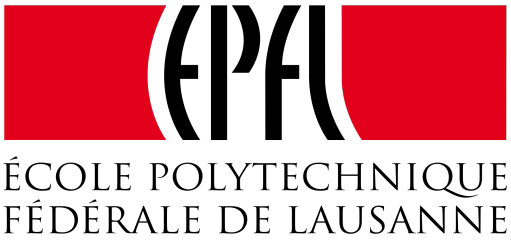

Contents

1 Introduction

Abdominal aortic aneurysms (AAA) is a pathology that cause 1 to 3% of the deaths among men aged between 65 and 85 in developed countries. By *aneurysm* it is meant an irreversible localized dilatation of a blood vessel. In the case of AAA, this dilatation is located in the region of aorta between the renal arteries and the iliac bifurcation. The maximal section of the aneurysm has a diameter between 15 and 24 cm, which is above 1.5 times the normal diameter of the abdominal aorta. The major risk associated to AAA is rupture, often caused by traumas, which leads to death in 65% of the cases [1].

Since open repairing of AAA is an invasive procedure, a number of alternative treatment options have been proposed. Among these, endovascular aneurysm sealing (EVAS) is a technology that has evolved during the last 3 to 5 years and consists of filling the AAA sac with a polymer (called *sealing*). The Nellix[1] EVAS device used for intervention consists of two identical catheter-based devices with a 10mm flow-lumen created by two baloons-expandible stents. The two stents are fixed within the aneurysm using endobags which are filled with a polymer that adapts to the geometry of the aneurysm [2]. Therefore, once the intervention has ended with success, the lumen of the aneurysm is filled by the sealing and the blood pumped by the heart reaches first the region above the aneurysm (called *neck*), flows through the stents and continues its physiological flow in the iliac arteries. Figure 2 represents the device once it has been placed.

However, EVAS is still an experimental procedure, therefore needs further validation. In this context numerical simulations may be a suitable tool to predict what consequences the device has on the blood flow once it has been placed.

The first aim of the present project is to set up and run numerical simulations of the blood flow in a section of abdominal aorta in two situations:

- Pre-operational setting, i.e. in presence of a developed aneurysm before intervention;
- Post-operational setting, i.e. after intervention, once stents and sealing have been placed.

Secondly, results obtained from the simulations are post-processed to obtain a quantitative comparison between the pre and post-operational conditions. In particular, the quantities of interest considered are:

- wall shear stress (WSS), its time average (TAWSS), oscillatory shear index (OSI) and endothelial cell activation potential (ECAP) (whose exact definition and physical meaning are given in the next section) are computed to quantify the impact of the EVAS device on the neck and in particular determine if its presence may cause pathologies such as the formation of intraluminal thrombi;
- pressure drops between abdominal aorta and iliac arteries are compared between the pre and post-operational setting. The relevance of this quantity can be noticed drawing a parallelism with the study of *stenoses* (i.e. an abnormal narrowing of a blood vessel), in which a key descriptive parameter is the pressure drop between an upper healthy section of the vessel and the stenotic region.

2 Mathematical model and quantities of interest

The mathematical models presented in this section are mainly based on [7], [8].

2.1 Navier-Stokes problem

The physical model employed to describe the flow of the blood is the one of incompressible Newtonian fluids. Incompressible Navier-Stokes equations are therefore employed to determine the velocity field $\boldsymbol{u}$ and pressure

[1] https://endologix.com/international/products/nellix/

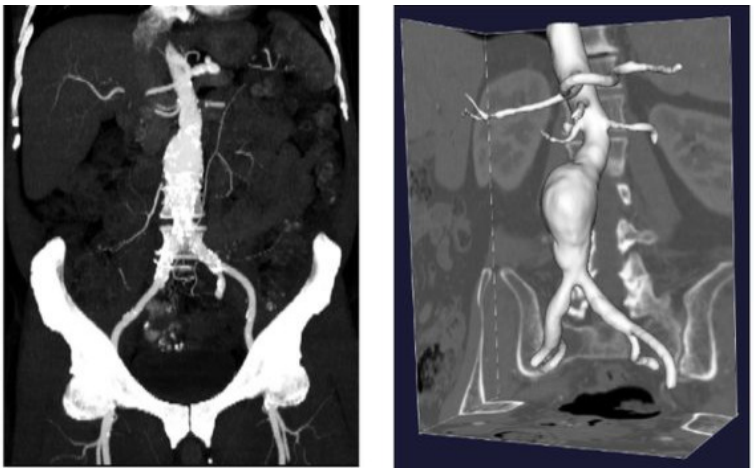

Figure 1: On the left, a scan of an abdominal aortic aneurysm obtained with CTA, on the right a 3 dimensional reconstruction of its geometry. Source: [4]

p of a fluid flow as a PDE which, in a general setting, has the following form:

$$\begin{aligned}
&\rho\frac{\partial \boldsymbol{u}}{\partial t} + \rho\boldsymbol{u}\cdot\boldsymbol{\nabla}\boldsymbol{u} - \boldsymbol{\nabla}\cdot\boldsymbol{\sigma}(\boldsymbol{u},p) = \boldsymbol{f} \text{ in } \Omega\times[0,T],\\
&\boldsymbol{\nabla}\cdot\boldsymbol{u} = 0 \text{ in } \Omega\times[0,T],\\
&\boldsymbol{u} = \boldsymbol{g}_D \text{ on } \Gamma_D\times[0,T],\\
&\frac{\partial \boldsymbol{u}}{\partial \boldsymbol{n}} = \boldsymbol{g}_N \text{ on } \Gamma_N\times[0,T],\\
&\boldsymbol{u} = \boldsymbol{u_0} \text{ on } \Omega\times\{0\},
\end{aligned} \tag{1}$$

where $\Omega\subset\mathbb{R}^3$ is a spatial region with piecewise smooth boundary Γ and $T\in\mathbb{R}$ is the final time. Let $\Gamma = \Gamma_D\cup\Gamma_N$ with $\Gamma_D\cap\Gamma_N = \emptyset$, i.e. the boundary of Ω is partitioned in two regions where Dirichlet and Neumann boundary conditions respectively are enforced (here denoted respectively by $\mathbf{g_D}$ and $\mathbf{g_N}$ respectively). $\rho\in\mathbb{R}_+$ represents the density of the fluid and $\boldsymbol{f}$ a forcing term. The quantity $\boldsymbol{\sigma}(\boldsymbol{u},p)$ is the stress tensor defined as:

$$\boldsymbol{\sigma}(\boldsymbol{u},p) := -p\boldsymbol{I} + 2\mu\boldsymbol{D}(\boldsymbol{u}) \tag{2}$$

where I is the two-rank identity tensor, $\mu\in\mathbb{R}_+$ is the dynamical viscosity (constant from the assumption that the fluid is Newtonian) and D is the rate of deformation (or strain) tensor:

$$\boldsymbol{D} := \frac{1}{2}(\boldsymbol{\nabla}\boldsymbol{u} + \boldsymbol{\nabla}\boldsymbol{u}^T)$$

Finally, $\boldsymbol{u_0}$ represents the initial condition of the problem.

2.2 Weak formulation of the Navier-Stokes problem

In view of the finite elements approximation of the problem, we consider the following linear spaces:

$$\begin{aligned}
&V_g := \left\{\boldsymbol{v}\in\{H^1(\Omega)\}^3 : \boldsymbol{v}_{|\Gamma_D} = \boldsymbol{g}_D\right\},\ V_0 := \left\{\boldsymbol{v}\in\{H^1(\Omega)\}^3 : \boldsymbol{v}_{|\Gamma_D} = \boldsymbol{0}\right\},\\
&Q := L^2(\Omega),\\
&\mathcal{V}_g := V_g\times Q,\ \mathcal{V}_0 := V_0\times Q
\end{aligned}$$

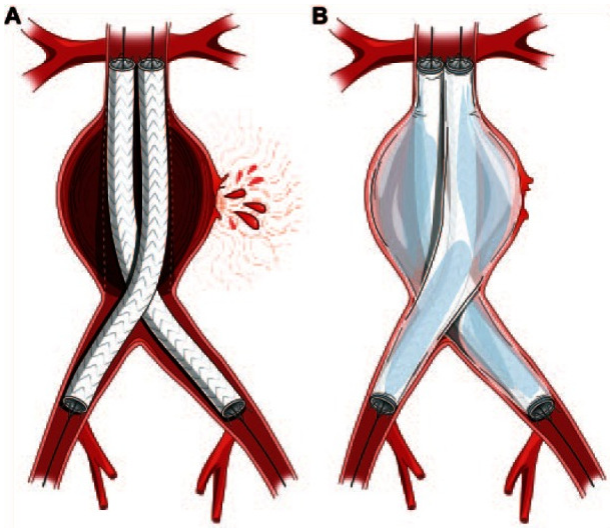

Figure 2: On the left, the Nellix stents deployed within a ruptured infrarenal aneurysm, with the endobags not inflated. On the right, the Nellix device fully deployed with hemostatic control of the rupture and perfusion to both limbs. Source: [2]

and the weak formulation of (1), which reads:

$$\begin{aligned}
&\forall t \in [0,T], \text{ find } \boldsymbol{U}(t) = (\boldsymbol{u}, p) \in \mathcal{V}_g : \\
&(\rho \frac{\partial \boldsymbol{u}}{\partial t}, \boldsymbol{v}) + (\rho \boldsymbol{u} \cdot \boldsymbol{\nabla} \boldsymbol{u}, \boldsymbol{v}) + (\mu(\boldsymbol{\nabla} \boldsymbol{u} + \boldsymbol{\nabla} \boldsymbol{u}^T), \boldsymbol{\nabla} \boldsymbol{v}) - (p, \boldsymbol{\nabla} \cdot \boldsymbol{v}) + (\boldsymbol{\nabla} \cdot \boldsymbol{u}, q) = \\
&= (\boldsymbol{f}, \boldsymbol{v}) + (\boldsymbol{g}_N, \boldsymbol{v})_{\Gamma_N} \qquad \forall \boldsymbol{V} = (\boldsymbol{v}, q) \in \mathcal{V}_0, \\
&\text{with } \boldsymbol{u}(0) = \boldsymbol{u}_0
\end{aligned} \tag{3}$$

where $(\cdot, \cdot)$ represents the scalar product of $H^1(\Omega)$ and $(\cdot, \cdot)_{\Gamma_N}$ the scalar product on $H^{\frac{1}{2}}(\Gamma_N)$.
The previous weak problem can be written in a more compact way as follows:

$$\begin{aligned}
&\forall t \in [0,T], \text{ find } \boldsymbol{U}(t) = (\boldsymbol{u}, p) \in \mathcal{V}_g : \\
&a_1(\boldsymbol{U}, \boldsymbol{V}) + a_2(\boldsymbol{U}, \boldsymbol{U}, \boldsymbol{V}) = F(\boldsymbol{V}) \qquad \forall \boldsymbol{V} = (\boldsymbol{v}, q) \in \mathcal{V}_0 \\
&\text{with } \boldsymbol{u}(0) = \boldsymbol{u}_0.
\end{aligned} \tag{4}$$

where, considering $\boldsymbol{W} = (\boldsymbol{w}, r) \in \mathcal{V}_g$,

$$\begin{aligned}
&a_1(\boldsymbol{U}, \boldsymbol{V}) := (\rho \frac{\partial \boldsymbol{u}}{\partial t}, \boldsymbol{v}) + (\mu(\boldsymbol{\nabla} \boldsymbol{u} + \boldsymbol{\nabla} \boldsymbol{u}^T), \boldsymbol{\nabla} \boldsymbol{v}) - (p, \boldsymbol{\nabla} \cdot \boldsymbol{v}) + (\boldsymbol{\nabla} \cdot \boldsymbol{u}, q), \\
&a_2(\boldsymbol{W}, \boldsymbol{U}, \boldsymbol{V}) := (\rho \boldsymbol{w} \cdot \boldsymbol{\nabla} \boldsymbol{u}, \boldsymbol{v}), \\
&F(\boldsymbol{V}) := (\boldsymbol{f}, \boldsymbol{v}) + (\boldsymbol{g}_N, \boldsymbol{v})_{\Gamma_N}.
\end{aligned} \tag{5}$$

This splitting of the left-hand side of (4) is meant to highlight the presence of a linear term (a_1) and a nonlinear term expressed through a trilinear form with two identical arguments(a_2).

2.3 Description of the domain and of the boundary conditions

Figure 3 depicts the domains of the pre and post-operational problems (actually, the computational mesh that are used for the numerical simulations). The geometry of (the surface of) the pre-operational problem is composed of 3 regions depending on the kind of boundary condition that is enforced on them:

- INLET (in figure 3, the top surface): non-homogeneous Dirichlet boundary condition. This boundary condition models the blood flow on this surface;

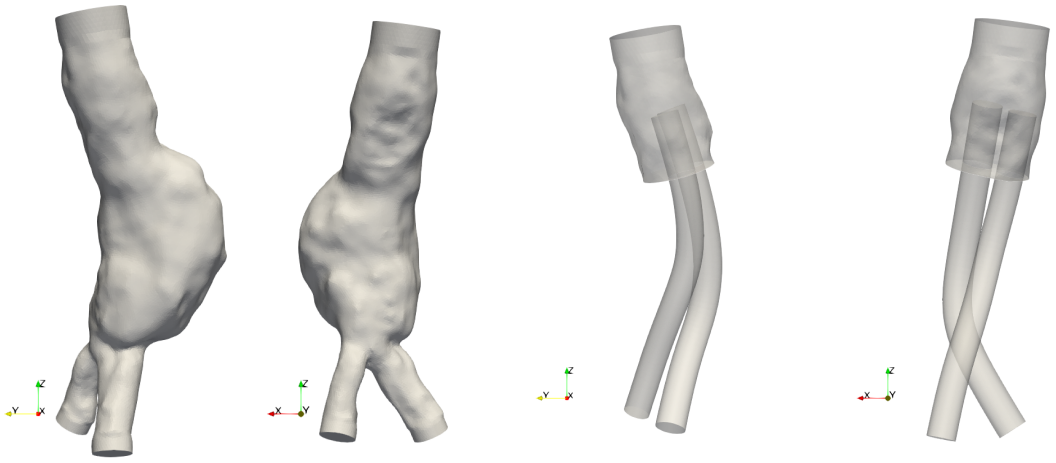

(a) (b) (c) (d)

Figure 3: Computational meshes used in the simulation. (a) and (b) represent the pre-operational mesh from two perspectives, (c) and (d) the same for the post-operational mesh with a partial opacity to display the internal structure of the domain.

- WALL (the mesh of the aorta wall): homogeneous Dirichlet boundary condition. This region, which represents the interface with the aorta wall, is assigned a no-slip boundary condition;
- OUTLET (in figure 3, the bottom surfaces): homogeneous Neumann boundary condition. This (disjoint) region represents the interface between the domain and the continuation of the iliac arteries.

As for the post-operational mesh, the geometry is slightly more complex:

- INLET: as in the pre-operational problem;
- WALL1, WALL2, WALL3, WALL4: homogeneous Dirichlet boundary condition. These regions, which represent the stent above and below the top sealing surface (respectively WALL1 and WALL2), the interface with the aorta wall (WALL3) and the interface with the sealing (WALL4), are assigned a no-slip boundary conditions;
- OUTLET: as in the pre-operational problem.

It is remarked that the regions of boundary WALL in the pre-operational mesh and WALL3 in the post-operational one are approximated by a *rigid* surface, while in reality the compliance of the vessel's wall has an effect on the blood flow (see the final section for more details). As a consequence, also the no-slip boundary condition enforced on these surfaces is an approximation. By contrast, the no-slip boundary condition defined on WALL1 and WALL2 represents more precisely the physical problem, as these surfaces can be considered rigid.

As for the non-homogeneous Dirichlet boundary condition (the same in both pre and post-operational problem) mentioned above, a *Womersley velocity profile* [6] is chosen to prescribe the velocity field on INLET (in both pre and post-operational settings). This analytical description of a velocity field driven by a pulsating pressure gradient in a cylindrical vessel is a function of several non-dimensional quantities and can be easily expressed as a function of the flow-rate of the velocity fields. More precisely, it can be defined as:

$$\begin{aligned} &\boldsymbol{w} : \Theta \times [0,T] \to \mathbb{R}^3 \\ &\boldsymbol{w}(\rho,t) := \frac{Q(t)\omega}{\alpha^2\nu\pi}\left(1 - \frac{J_0(\alpha\gamma i^{\frac{3}{2}})}{J_0(\alpha i^{\frac{3}{2}})}\right)\left(1 - \frac{2J_1(\alpha i^{\frac{3}{2}})}{\alpha i^{\frac{3}{2}} J_0(\alpha i^{\frac{3}{2}})}\right)^{-1} \end{aligned} \tag{6}$$

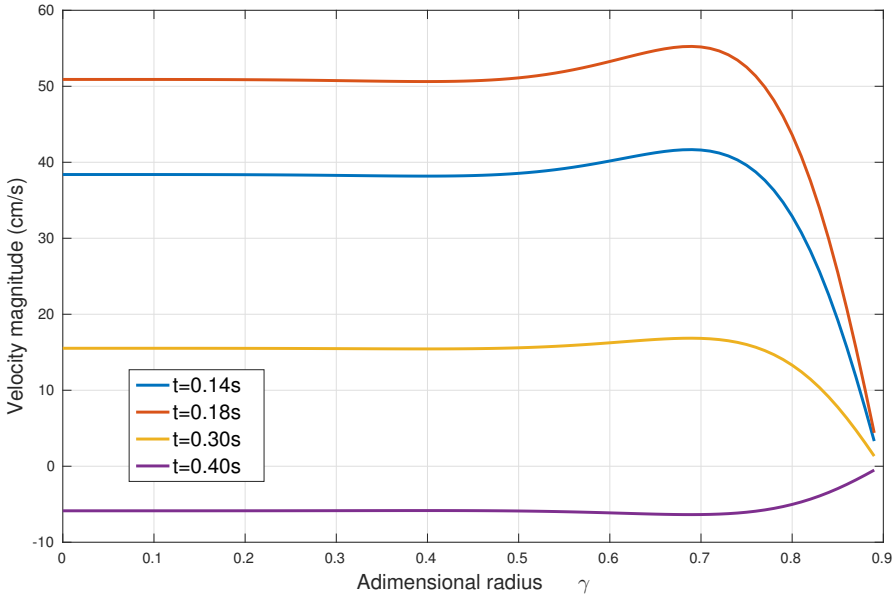

Figure 4: Plot of the Womersley profile at different times as a function of the adimensional radius γ (the velocity profile has radial symmetry). All the parameters of the velocity profile are chosen as in the numerical experiments described in the following sections. In particular, the flow-rate is the one depicted in figure 6.

where Θ is a section of the vessel (approximately a circle of radius R) on which we fix a polar coordinate reference system (ρ, θ) (the expression of $\boldsymbol{w}$ does not depend on θ), $Q(t)$ is the flow-rate of the blood through Θ or, more precisely:

$$\begin{aligned} &Q : [0, T] \to \mathbb{R} \\ &Q(t) := \int_{\Theta} \boldsymbol{w}(\rho, t) \mathrm{d}\Sigma, \end{aligned} \tag{7}$$

$\omega := 2\pi f$ is the "angular frequency" of the pulsating periodic flow (f is the frequency of the pulsation), $\alpha := \sqrt{\frac{R^2\omega}{\nu}}$ is a non-dimensional parameter called Womersley number, $\gamma := \frac{\rho}{R}$ is the non-dimensional radius and J_0 and J_1 are Bessel functions of the first kind. We remark that in (6) the real part of the expression is considered. Figure 4 shows a plot of a typical Womersley velocity profile at different times during a heart-beat.

The homogeneous Neumann boundary condition on OUTLET is chosen to fix the value of p (which otherwise would be unique only up to a constant) in the (disjoint) region of boundary OUTLET (in both pre and post operational problems). It must be remarked that this choice is an approximation. Indeed, the two disjoint regions that constitute OUTLET neither lay on the same place nor are at the same z-coordinate however, due to their proximity and similar orientation, this approximation can be accepted.

The initial condition is chosen as $\boldsymbol{u}_0 = \boldsymbol{0}$ on Ω, since no physically relevant initial condition is available. We remark that because of this choice the simulation will present a "false" transient component linked to the incorrect initial condition. However, this transient component is assumed to rapidly decays and after a time equal to one or two heart beats the solution can be considered not influenced anymore by the incorrect initial data.

Finally, it should be remarked that the portion on boundary WALL1 differs from the others for its property of being "internal" (i.e. the interior of the domain Ω lays on both of its sides). This situation arises from the fact that, due to its negligible thickness, the surface of the stent is "collapsed" to a cylindrical surface (*shell*). This approximation does not have consequences on the simulation as homogeneous Dirichlet boundary conditions are enforced in this region. Indeed, if the stent is not approximated as a shell, we can

consider its internal and external surfaces Γ^1_{W1} and Γ^2_{W1}. Then, the boundary integral that arises in the derivation of the weak problem (3) can be written, in this region, as:

$$\int_{\Gamma^1_{W1}} \left(p\boldsymbol{n} - \nu \frac{\partial \boldsymbol{u}}{\partial \boldsymbol{n}} \right) \cdot \boldsymbol{v} d\partial\Omega + \int_{\Gamma^2_{W1}} \left(p\boldsymbol{n} - \nu \frac{\partial \boldsymbol{u}}{\partial \boldsymbol{n}} \right) \cdot \boldsymbol{v} d\partial\Omega$$

and its value is 0 due to the fact that $\boldsymbol{v} \in V_0$. For the same reason, also reducing the number of degrees of freedom of the finite elements solutions (that will be described in the next chapter) does not have any consequence.

2.4 Quantites of interest

As mentioned in the previous section, there are some quantities that can help to quantify the difference between the pre and post operational settings and that are described in this section. This section is partially based on [4].

Wall shear stress (WSS) is defined as:

$$\boldsymbol{\tau}_W(\boldsymbol{x}, t) := \boldsymbol{\sigma}\boldsymbol{n} - ((\boldsymbol{\sigma}\boldsymbol{n}) \cdot \boldsymbol{n})\, \boldsymbol{n} \; \forall \boldsymbol{x} \in \partial\Omega, t \in [0, T] \tag{8}$$

where $\boldsymbol{\sigma} = \boldsymbol{\sigma}(\boldsymbol{x}, t)$ is the stress tensor defined as in (2) and $\boldsymbol{n} = \boldsymbol{n}(\boldsymbol{x})$ is the outward normal unit vector to $\partial\Omega$. If computed at the interface of the fluid with a surface, taking $\boldsymbol{n}(\boldsymbol{x})$ as the normal unit vector to the surface, WSS can be interpreted as the *shear* (i.e. parallel to the surface) force exerted by the fluid on the surface. WSS is computed on the whole section of abdominal aorta in the pre-operational setting and on the upper section of the blood vessel in the post-operational one to asses whether or not the presence of the stent causes the upper section of the abdominal aorta to be subject to pathological stresses.

As WSS is a function of time, it could be synthesized further through a time–average (TAWSS):

$$\text{TAWSS}(\boldsymbol{x}) = \frac{1}{T} \int_0^T |\boldsymbol{\tau}_W(\boldsymbol{x}, t)|\, dt,$$

being T here the period of the heartbeat.

Oscillatory shear index (OSI) is defined as follows:

$$\text{OSI}(\boldsymbol{x}) := \frac{1}{2} \left(1 - \frac{\left| \int_0^T \boldsymbol{\tau}_W dt \right|}{\int_0^T |\boldsymbol{\tau}_W|\, dt} \right) \; \forall \boldsymbol{x} \in \Omega$$

and assumes its maximum (0.5) in regions where the flow's oscillatory behavior is dominant compared to its intensity. For instance a purely oscillatory motion will give an OSI of 0.5 while an unidirectional flow in a regular geometry will give OSI= 0.

It is desirable to locate the regions of the vessel wall that are subjected to high OSI and low TAWSS (therefore where on average the flow varies direction frequently and where its magnitude is small), we define the following quantity that, following [4], is called *endothelial cell activation parameter* (ECAP):

$$\text{ECAP} := \frac{\text{OSI}}{\text{TAWSS}}.$$

The relevance of this quantity comes from the fact that regions with a high ECAP are those that, on the long term, have higher probability of manifesting intraluminal thrombi.

Finally, pressure drops are computed between INLET and OUTLET in both pre and post-operational settings taking averages of pressure over these regions, i.e.:

$$\Delta p = \frac{1}{|\Gamma_{IN}|} \int_{\Gamma_{IN}} p(\boldsymbol{x}, t) d\Sigma - \frac{1}{|\,\Gamma_{OUT}|} \int_{\Gamma_{OUT}} p(\boldsymbol{x}, t) d\Sigma.$$

3 Mesh generation

The pre-operational surface mesh is obtained from medical images (MRI) through application of segmentation techniques. *Flow extensions* (i.e. cylindrical regions located at the ends of the mesh) are added to facilitate the imposition of boundary condition and reduce the dependence of the numerical solution on the model used to describe boundary conditions (in this case the Womersley flow model for the inflow).

The post-operational mesh consists of the region where the blood flows once the EVAS device is placed. A schematic representation is given in figure 5 (a). Its surface is obtained from the pre-operational mesh first using filters of *Paraview*[2], then re-meshing it with *Gmsh*[3], which is also used to obtain the volumetric mesh.
More specifically, meshes for the tubes that represent the stents of the medical device are generated from splines running from the neck of the aneurysm to each of the iliac arteries. The tubes are then built around the splines using a fixed diameter chosen to match the maximum diameter that can fit both iliac arteries. After this, the pre-operational mesh is clipped to obtain a surface that only encloses the region of lumen above the sealing. Next, a new surface is generated taking the *difference* of the surface of the region above the sealing with the two tubes. Then, starting from this surface and the tubes, three volumetric meshes are obtained (figure 5(b)) and eventually assembled into the final computational mesh. To obtain a *conformal* mesh, care must be taken to generate the same surface grid for the volumetric meshes that will be merged in the assembling phase. More precisely, surface meshes must be the same up to the tolerance of the function of the software used to perform this operations (in the present case, *Gmsh*).

Some remarks must be made about the post-operational mesh. The fact that several part of the domain (tubes and interface with the sealing) are obtained "artificially" and not through medical data may pose limitations to the comparison with a real blood flow. More specifically, while in the actual EVAS device stents are placed one next to the other, the post-operational mesh is composed of two tubes separated by a small gap. Secondly, the length of the section of the tubes that is not surrounded by the sealing is sensibly longer than in the real device. Thirdly, the top surface of the sealing is approximated with a plane.
The approximations listed above are motivated by the fact that segmenting the surgical device (especially the surface of the sealing) from medical images is still a problematic task.

Finally, we remark that despite these geometrical approximations the current mesh contains all the characterizing (geometrical) features of the problem. Moreover, in case post-operational images were available, the centerlines of the tubes (splines) could be defined starting from these, then the rest of the mesh could be built following the same procedure described above.

4 Numerical scheme

The weak problem (3) is approximated (in space) through a finite elements scheme with either VMS-LES (Variational Multi Scale - Large Eddy Simulation) stabilization or SUPG. Then, a fully discrete scheme is obtained through a further discretization (in time) which, in this case, is performed using a semi-implicit BDF scheme with extrapolation using Newton-Gregory polynomials. This section, based on [8], present a step-by-step derivation of the fully discrete scheme that is used in the simulations.

4.1 Finite-elements approximation

Let us first introduce the Galerkin approximation of (3). Consider V_g^h, V_0^h and Q^h, finite dimensional subspaces of V_g, V_0 and Q respectively and $\mathcal{V}_g^h := V_g^h \times Q^h$, $\mathcal{V}_0^h := V_0^h \times Q^h$. The Galerkin approximation

[2] https://www.paraview.org/
[3] http://gmsh.info/

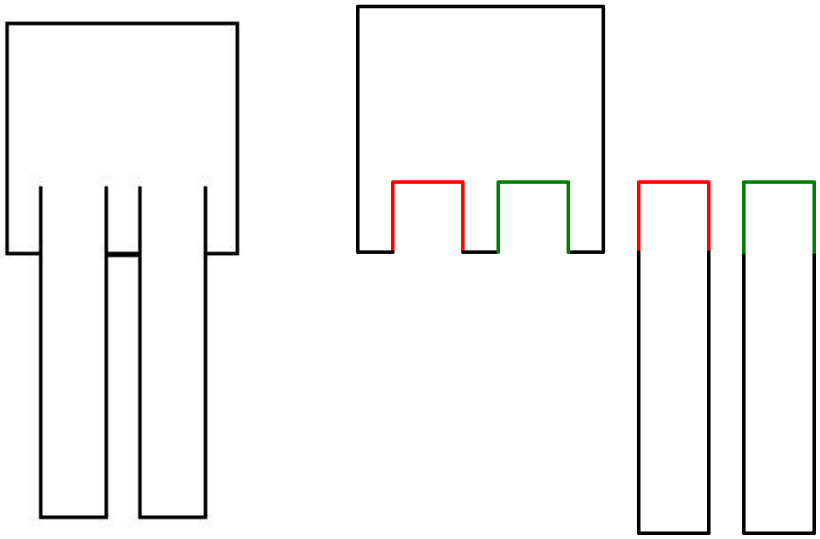

(a) (b)

Figure 5: (a): Schematic representation of (a section of) the post-operational surface mesh; (b): representation of the three volumetric meshes to be assembled. In red and green the the subsets of the boundary where meshes must "match" to obtain a global conformal mesh.

of (3) reads:

$$\begin{aligned}
&\forall t \in [0,T], \text{ find } \boldsymbol{U^h}(t) = (\boldsymbol{u}^h, p^h) \in \mathcal{V}_g^h : \\
&(\rho \frac{\partial \boldsymbol{u}^h}{\partial t}, \boldsymbol{v}^h) + (\rho \boldsymbol{u}^h \cdot \boldsymbol{\nabla} \boldsymbol{u}^h, \boldsymbol{v}^h) + (\mu(\boldsymbol{\nabla} \boldsymbol{u}^h + (\boldsymbol{\nabla} \boldsymbol{u}^h)^T), \boldsymbol{\nabla} \boldsymbol{v}^h) - (p^h, \boldsymbol{\nabla} \cdot \boldsymbol{v}^h) + (\boldsymbol{\nabla} \cdot \boldsymbol{u}^h, q^h) = \\
&= (\boldsymbol{f}^h, \boldsymbol{v}^h) + (\boldsymbol{g}_N^h, \boldsymbol{v}^h)_{\Gamma_N} \qquad \forall \boldsymbol{V}^h = (\boldsymbol{v}^h, q^h) \in \mathcal{V}_0^h, \\
&\text{with } \boldsymbol{u}^h(0) = \boldsymbol{u}_0^h
\end{aligned} \tag{9}$$

or, more synthetically as in (4),

$$\begin{aligned}
&\forall t \in [0,T], \text{ find } \boldsymbol{U^h}(t) = (\boldsymbol{u}^h, p^h) \in \mathcal{V}_g^h : \\
&a_1(\boldsymbol{U}^h, \boldsymbol{V}^h) + a_2(\boldsymbol{U}^h, \boldsymbol{U}^h, \boldsymbol{V}^h) = F(\boldsymbol{V}^h) \qquad \forall \boldsymbol{V}^h = (\boldsymbol{v}^h, q^h) \in \mathcal{V}_0^h \\
&\text{with } \boldsymbol{u}^h(0) = \boldsymbol{u}_0^h,
\end{aligned} \tag{10}$$

where a_1, a_2 and F are defined as in (5), and $\boldsymbol{f}^h$, $\boldsymbol{h^h}$ and $\boldsymbol{u}_0^h$ are suitable approximations of $\boldsymbol{f}$, $\boldsymbol{g}_N$ and $\boldsymbol{u}_0$ respectively.

Secondly, the finite elements approximation of (3) is performed choosing the following linear subspaces:

$$V_g^h := \{X_r^h\}^d \cap V_g(\Omega_h), \; V_0^h := \{X_r^h\}^d \cap V_0(\Omega_h), \; Q^h := X_r^h \cap Q(\Omega_h)$$

being Ω_h the union of the elements of a triangulation $\mathcal{T}_h$ of Ω and

$$X^h(\Omega_h) := \{\boldsymbol{v} \in C^0(\Omega_h) : \boldsymbol{v}_{|h} \in \mathbb{P}^r(K) \; \forall K \in \mathcal{T}_h\}$$

the linear space of piecewise polynomial functions of degree r on each element K of $\mathcal{T}_h$.

4.2 VMS-LES stabilization

The VMS-LES stabilization of the problem is introduced by first considering a new linear space for the solutions:

$$\mathcal{V} = \mathcal{V}^h \oplus \mathcal{V}',$$

where the finite elements space $\mathcal{V}^h$ represents the "coarse scale", while $\mathcal{V}'$ represents the "fine scale" of the solution. Therefore, we have a decomposition of the solution and the test functions of (10) as:

$$\begin{aligned}\boldsymbol{u} &= \boldsymbol{u}^h + \boldsymbol{u}',\\ p &= p^h + p',\\ \boldsymbol{v} &= \boldsymbol{v}^h + \boldsymbol{v}',\\ q &= q^h + q'.\end{aligned}$$

The fine-scale components of the solution are *modeled* as follows:

$$\begin{aligned}\boldsymbol{u}' &:= -\tau_M(\boldsymbol{u}^h)\boldsymbol{r}_M(\boldsymbol{u}, p^h),\\ p' &:= -\tau_C(\boldsymbol{u}^h) r_C(\boldsymbol{u}^h)\end{aligned}$$

where $\boldsymbol{r}_M$ and r_C represent the strong residuals of momentum and continuity equations respectively and τ_m and τ_C are stabilization parameters chosen as follows:

$$\begin{aligned}\tau_M = \tau_M(\boldsymbol{u}^h) &= \left(\frac{\sigma^2\rho^2}{\Delta t^2} + \frac{\rho^2}{h_k^2}|\boldsymbol{u}^h|^2 + \frac{\mu^2}{h_K^4}C_r\right)^{-\frac{1}{2}},\\ \tau_C = \tau_C(\boldsymbol{u}^h) &= \frac{h_k^2}{\tau_M(\boldsymbol{u}^h)}\end{aligned}$$

where σ is the order of the time discretization (a constant), Δt is the time discretization step, h_k is the upper bound of the diameter of the element $K \in \mathcal{T}_h$ and $C_r := 60 \cdot 2^{r-2}$ is a constant obtained by an inverse inequality relation.
Finally, the VMS-LES semi-discrete approximation of Navier-Stokes equations reads:

$$\begin{aligned}&\text{Find } \boldsymbol{U}^h(t) = (\boldsymbol{u}^h, p^h) \in \mathcal{V}_g^h :\\ &a_1(\boldsymbol{U}^h, \boldsymbol{V}^h) + a_2(\boldsymbol{U}^h, \boldsymbol{U}^h, \boldsymbol{V}^h) + a_{VMS}^h(\boldsymbol{U}^h, \boldsymbol{V}^h) = F(\boldsymbol{V}^h) \qquad \forall \boldsymbol{V}^h = (\boldsymbol{v}^h, q^h) \in \mathcal{V}_0^h\\ &\text{with } \boldsymbol{u}^h(0) = \boldsymbol{u}_0^h,\end{aligned} \tag{11}$$

with

$$\begin{aligned}a_{VMS}^h(\boldsymbol{U}^h, \boldsymbol{V}^h) := &\left(\rho\boldsymbol{u}^h \cdot \boldsymbol{\nabla}\boldsymbol{v}^h + \boldsymbol{\nabla}q^h, \tau_M(\boldsymbol{u}^h)\boldsymbol{r}_M(\boldsymbol{u}^h, p^h)\right) +\\ &- \left(\boldsymbol{\nabla}\cdot\boldsymbol{v}^h, \tau_C(\boldsymbol{u}^h)\boldsymbol{r}_C(\boldsymbol{u}^h)\right) +\\ &+ \left(\rho\boldsymbol{u}^h \cdot (\boldsymbol{\nabla}\boldsymbol{u}^h)^T, \tau_M(\boldsymbol{u}^h)\boldsymbol{r}_M(\boldsymbol{u}^h, p^h)\right) +\\ &- \left(\boldsymbol{\nabla}\boldsymbol{v}^h, \tau_M(\boldsymbol{u}^h, p^h) \otimes \tau_M(\boldsymbol{u}^h)\boldsymbol{r}_M(\boldsymbol{u}^h, p^h)\right).\end{aligned} \tag{12}$$

The first two lines correspond to the SUPG stabilization, the last two are characteristic of the VMS-LES stabilization.

4.3 SUPG stabilization

An alternative to the VMS-LES stabilization presented in the previous section is the streamline upwind Petrov Galerkin (SUPG) stabilization [9]. The finite elements approximation with SUPG stabilization can be written as (11):

$$\begin{aligned}&\text{Find } \boldsymbol{U}^h(t) = (\boldsymbol{u}^h, p^h) \in \mathcal{V}_g^h :\\ &a_1(\boldsymbol{U}^h, \boldsymbol{V}^h) + a_2(\boldsymbol{U}^h, \boldsymbol{U}^h, \boldsymbol{V}^h) + a_{SUPG}^h(\boldsymbol{U}^h, \boldsymbol{V}^h) = F(\boldsymbol{V}^h) \qquad \forall \boldsymbol{V}^h = (\boldsymbol{v}^h, q^h) \in \mathcal{V}_0^h\\ &\text{with } \boldsymbol{u}^h(0) = \boldsymbol{u}_0^h,\end{aligned} \tag{13}$$

where a_{VMS}^h is substituted by:

$$\begin{aligned}a_{SUPG}^h(\boldsymbol{U}^h, \boldsymbol{V}^h) := &\left(\rho\boldsymbol{u}^h \cdot \boldsymbol{\nabla}\boldsymbol{v}^h + \boldsymbol{\nabla}q^h, \tau_M(\boldsymbol{u}^h)\boldsymbol{r}_M(\boldsymbol{u}^h, p^h)\right) +\\ &- \left(\boldsymbol{\nabla}\cdot\boldsymbol{v}^h, \tau_C(\boldsymbol{u}^h)\boldsymbol{r}_C(\boldsymbol{u}^h)\right)\end{aligned} \tag{14}$$

using the notation introduced in the previous section. Observe that (14) consists of the first two summands of (12).

On one side, applying the SUPG stabilization leads to not as accurate results as VMS-LES (which also models the effect of a "fine scale" solution on the large scale one), on the other the former is computationally cheaper than the latter. This trade-off will be discussed again in section 6.

In the following section a fully discrete formulation of the problem is presented starting from the semi-discrete problem with VMS-LES stabilization. The equivalent SUPG-stabilized fully discrete formulation can be obtained eliminating the terms that arise from the summands in (12) that are not in (14).

4.4 Fully discrete problem through semi-implicit BDF scheme and second order extrapolation

A fully discrete approximation of the Navier-Stokes equations is achieved performing a discretization of the time-derivative of $\boldsymbol{u}^h$. To this end, the interval $[0,T]$ is split in $N \in \mathbb{N}$ subintervals of length $\Delta t = \frac{T}{N}$ each, divided by the $N+1$ temporal nodes $t_n := n \cdot \Delta t \ \forall 0 \leq n \leq N$. The valued of $\boldsymbol{u}^h$ is denoted $\boldsymbol{u}^h_n := \boldsymbol{u}^h(t_n)$ and $p^h_n := p^h(t_n)$.

A BDF (Backward Differentiation Formula) scheme is chosen to perform the time discretization. The approximation of the time-derivative of $\boldsymbol{u}^h$ can be expressed by a general formula:

$$\frac{\partial \boldsymbol{u}^h}{\partial t} \cong \frac{\alpha_\sigma \boldsymbol{u}^h_{n+1} - \boldsymbol{u}^h_{n\mathrm{BDF}\sigma}}{\Delta t}$$

where the parameters α_σ and $\boldsymbol{u}^h_{n\mathrm{BDF}\sigma}$ depend on the order of the BDF scheme σ. For instance for BDF2 we have $\alpha_2 := \frac{3}{2}$ and $\boldsymbol{u}^h_{n\mathrm{BDF}\sigma} := 2\boldsymbol{u}^h_n - \frac{1}{2}\boldsymbol{u}^h_{n-1}$ if $n \geq 1$. As it can be seen in the case of BDF2, BDF schemes are multi-step methods and the number of steps and the order of convergence are equal to its order σ.

Applying this time discretization to equation (11) at time t_{n+1} a *nonlinear* system of equations in the unknowns $\boldsymbol{u}^h_{n+1}$ and p^h_{n+1} is obtained. This could be solved numerically with a fully implicit approach, which has the advantage of yielding an unconditionally stable scheme, for example through Newton method. However, the downside of implicit schemes is their possibly prohibitive computational cost.

Therefore, with the aim of containing the computational cost associated to the simulation, a *semi-implicit* BDF scheme is considered. In particular, nonlinear terms depending on $\boldsymbol{u}^h_{n+1}$, p^h_{n+1} are extrapolated through Newton-Gregory backward polynomials. These extrapolations read, for the order 2:

$$\begin{aligned} \boldsymbol{u}^h_{n+1,\sigma} &:= 2\boldsymbol{u}^h_n - \boldsymbol{u}^h_{n-1}, \\ p^h_{n+1,\sigma} &:= 2p^h_n - p^h_{n-1}, \end{aligned}$$

with $n \geq 1$.

Thus, first applying an order σ BDF approximation of the time derivative and then an extrapolation of the same order on the *nonlinear* terms, the following problem is obtained at time t_{n+1}:

$$\begin{aligned}
&\text{Find } (\boldsymbol{u}^h_{n+1}, p^h_{n+1}) \in \mathcal{V}^h_g : \\
&\rho\left(\frac{\alpha_\sigma \boldsymbol{u}^h_{n+1} - \boldsymbol{u}^h_{n,\mathrm{BDF}\sigma}}{\Delta t}, \boldsymbol{v}^h\right) + \rho(\boldsymbol{u}^h_{n+1,\sigma} \cdot \boldsymbol{\nabla} \boldsymbol{u}^h_{n+1}, \boldsymbol{v}^h) + (\mu(\boldsymbol{\nabla} \boldsymbol{u}^h_{n+1} + (\boldsymbol{\nabla} \boldsymbol{u}^h_{n+1})^T), \boldsymbol{\nabla} \boldsymbol{v}^h) + \\
&- (p^h_{n+1}, \boldsymbol{\nabla} \cdot \boldsymbol{v}^h) + (\boldsymbol{\nabla} \cdot \boldsymbol{u}^h_{n+1}, q^h) + \\
&+ \left(\rho \boldsymbol{u}^h_{n+1,\sigma} \cdot \boldsymbol{\nabla} \boldsymbol{v}^h + \boldsymbol{\nabla} q^h, \tau^{n+1,\sigma}_M \boldsymbol{r}^{n+1,\sigma}_M(\boldsymbol{u}^h_{n+1}, p^h_{n+1})\right) - \left(\boldsymbol{\nabla} \cdot \boldsymbol{v}^h, \tau^{n+1,\sigma}_C \boldsymbol{r}_C(\boldsymbol{u}^h_{n+1})\right) + \\
&+ \left(\rho \boldsymbol{u}^h_{n+1,\sigma} \cdot (\boldsymbol{\nabla} \boldsymbol{v}^h)^T, \tau^{n+1,\sigma}_M \boldsymbol{r}^{n+1,\sigma}_M(\boldsymbol{u}^h_{n+1}, p^h_{n+1})\right) - \left(\boldsymbol{\nabla} \boldsymbol{v}^h, \tau^{n+1,\sigma}_M \hat{\boldsymbol{r}}^{n+1,\sigma}_M \otimes \tau^{n+1,\sigma}_M \tilde{\boldsymbol{r}}^{n+1,\sigma}_M(\boldsymbol{u}^h_{n+1}, p^h_{n+1})\right) + \\
&- \left(\boldsymbol{\nabla} \boldsymbol{v}^h, \tau^{n+1,\sigma}_M \hat{\boldsymbol{r}}^{n+1,\sigma}_M \otimes \tau^{n+1,\sigma}_M \rho \alpha_\sigma \frac{\boldsymbol{u}^h_{n+1}}{\Delta t}\right) + \left(\boldsymbol{\nabla} \boldsymbol{v}^h, \tau^{n+1,\sigma}_M \boldsymbol{r}^{n+1,\sigma}_M(\boldsymbol{u}^h_{n+1}, p^h_{n+1})) \otimes \tau^{n+1,\sigma}_M \rho \frac{\boldsymbol{u}^h_{n,BDF\sigma}}{\Delta t}\right) = \\
&= (\boldsymbol{f}_{n+1}, \boldsymbol{v}^h) + ((\boldsymbol{g}_N)_{n+1}, \boldsymbol{v}^h)_{\Gamma_N}; \\
&\text{with } \boldsymbol{u}^h(0) = \boldsymbol{u}^h_0;
\end{aligned}$$

where $\boldsymbol{u}^h_{n-\sigma+1}, ..., \boldsymbol{u}^h_n$ are given, $\boldsymbol{f}_{n+1} := \boldsymbol{f}(t_{n+1})$ and the modified stabilization parameters and residuals read:

$$\tau_M^{n+1,\sigma} = \left(\frac{\sigma^2\rho^2}{\Delta t^2} + \frac{\rho^2}{h_k^2}|\boldsymbol{u}^h_{n+1,\sigma}|^2 + \frac{\mu^2}{h_K^4}C_r \right)^{-\frac{1}{2}}, \ \tau_C = \frac{h_k^2}{\tau_M^{n+1,\sigma}};$$

$$\boldsymbol{r}_M^{n+1,\sigma}(\boldsymbol{u}^h_{n+1}, p^h_{n+1}) := \rho\frac{\alpha_\sigma \boldsymbol{u}^h_{n+1} - \boldsymbol{u}^h_{n,\mathrm{BDF}\sigma}}{\Delta t} + \rho\boldsymbol{u}^h_{n+1,\sigma}\cdot\boldsymbol{\nabla}\boldsymbol{u}^h_{n+1} + \boldsymbol{\nabla}p^h_{n+1} - \mu\Delta\boldsymbol{u}^h_{n+1} - \boldsymbol{f}_{n+1};$$

$$\hat{\boldsymbol{r}}_M^{n+1,\sigma} := \boldsymbol{r}_M^{n+1,\sigma}(\boldsymbol{u}^h_{n+1,\sigma}, p^h_{n+1,\sigma});$$

$$\tilde{\boldsymbol{r}}_M^{n+1,\sigma}(\boldsymbol{u}^h_{n+1}, p^h_{n+1}) := \rho\boldsymbol{u}^h_{n+1,\sigma}\cdot\boldsymbol{\nabla}\boldsymbol{u}^h_{n+1} + \boldsymbol{\nabla}p^h_{n+1} - \mu\Delta\boldsymbol{u}^h_{n+1} - \boldsymbol{f}_{n+1}.$$

This way a *linear* system is obtained at every time-step for the unknown vectors $\boldsymbol{u}^h_{n+1}$ and p^h_{n+1}. However, it must be remarked that this scheme, unlike the fully implicit ones, is not unconditionally stable, therefore particular attention must be taken in choosing the time-step.

Finally, some remarks about the method presented in this chapter:

- the choice of finite elements spaces for velocity and pressure of type $\mathbb{P}_i - \mathbb{P}_i$ (where $i \in \mathbb{N}$) leads to spurious modes for pressure in mixed problems approximated with classical finite elements due to the fact that the discrete inf-sup condition is not satisfied. However, thanks to the VMS-LES (or SUPG) stabilization, this choice of finite elements space leads to satisfactory results;
- in general, a semi-implicit BDF scheme of order n has order of convergence $\mathcal{O}(\Delta t^n)$ only if extrapolation is of order n or bigger, as a lower order extrapolation, say $m < n$, would cause the method to have only a $\mathcal{O}(\Delta t^m)$ convergence order.

5 Implementation

The numerical scheme described in the previous section is implemented in the module `navier_stokes_blocks` of the finite elements library *LifeV*[4] for the parallel solution of PDEs. This code is employed to run simulations of the problems addressed in the project. The code of a test of the `navier_stokes_blocks` module is used as the starting point for the development of the simulations on the blood vessel domain in pre and post-operational conditions. However, some modifications are needed to adapt it to the current problem. In particular:

- scaling of the mesh: the mesh, originally in mm, is scaled of a factor 1/10 (thus obtaining a mesh in cm) to adapt it to the desired dimension of the solution (i.e. $\frac{cm}{s}$ for the velocity and $\frac{dyn}{cm^2}$ for the pressure);
- imposition of boundary conditions on the "internal" boundary: as mentioned in section (2.3), the region of boundary WALL1 is "internal". As the current version of *LifeV* does not allow to impose boundary conditions on this kind of region through the standard methods used to handle boundary conditions, these are imposed through the use of other methods of the same classes. Particular care is taken in making the resulting code suitable for the parallel implementation with *OpenMPI*;
- class *VelocityProfile*: as the Womersley profile is a function of geometrical properties of the domain (i.e. radius, center and unit outward normal vector to the section of domain where they are imposed), a class called *VelocityProfile* is added to store information about this boundary condition. In particular, it stores geometrical information on the mesh through *static* class members and manages the analytical functions describing the Womersley profile and the flow-rate (as defined in (7)) through two class methods. The flowrate function, shown in figure 6, is computed using the *Curve fitting toolbox*[5] of *Matlab* interpolating sampled values from the literature [5]. More precisely, a 7th order Fourier expansion over the time interval $[0, 0.8s]$ is employed;

[4] www.lifev.org

[5] https://ch.mathworks.com/help/curvefit/

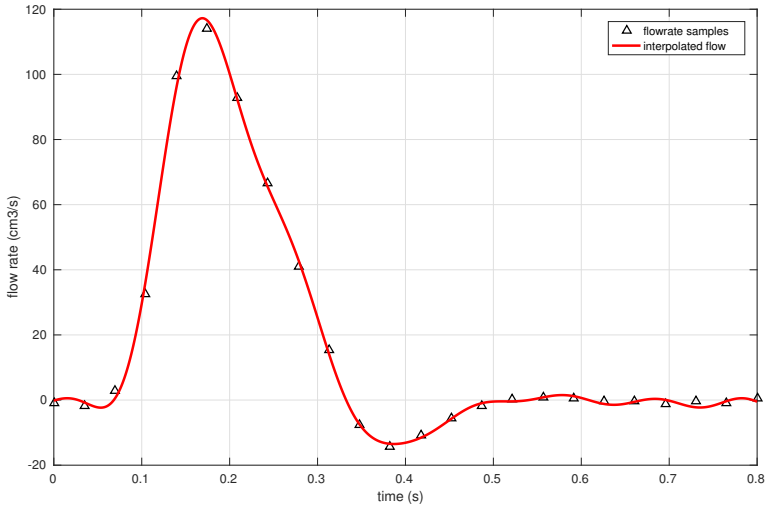

Figure 6: The flow-rate employed in the simulations, as a function of time. Triangles represents the interpolated samples.

- exporting of the solution every fixed number of time-steps (given through datafile). This option also takes into account the fact that BDF methods are implicit, therefore need as many initial values as their order to start a new computation;
- restart procedure: as the execution of the simulation on supercomputers may reach the maximum time allocated, a procedure is needed to start a new simulation from the results computed in the previous one. To this end, the code is added the option (that can be selected through datafile) to import from an *HDF5* format file as many final results as needed by the BDF solver (i.e. as many as the order of the BDF scheme);
- validation of parallel implementations: for every new feature added to the code, results of parallel and serial runs are compared on simplified problems to assess whether or not they produce the same results (up to the tolerance of the linear system solver). Results are compared using filters of *paraview* to produce time-plots of the error, expressed as (e.g. for pressure):

$$err_p(t) := \frac{\int_\Omega |p_s - p_p| d\Omega}{|\Omega| \cdot \int_\Omega |p_s| d\Omega}$$

  where p_s and p_p are numerical approximations of $p_s - p_p$ computed in serial and parallel, Ω is the domain and $|\Omega|$ is its size. With the same approach an error over the velocity field is defined, simply taking the modulus of $\boldsymbol{v}_s - \boldsymbol{v}_p$ instead of p in the previous definition.
- computation of WSS, TAWSS, OSI and pressure drops: after the simulation is run, its results are post-processed to compute the quantities described in section 2.4. This task is performed by a function that first imports the simulations results, then computes the quantities of interest and finally exports them to a new file;
- ECAP: values of ECAP are computed and visualized using filters of the visualization software *Paraview*;

6 Results

Simulations are performed using computational meshes with 420'303 and 264'530 vertices for the pre-operational and post-operational simulation respectively. The different number of vertices is due to the

different volume of the two domains (larger for the pre-operational mesh) and the grid size. The grid size is smaller for the post operational case (if we consider only the neck of the aneurysm in the two cases, it contains 102'446 vertices for the pre operational mesh ,170'606 for the post-operational one) to be able to mesh the narrow gap between the neck and the stents.

As for the physical parameter of the simulation, the density of the blood is fixed to $\rho = 1.06 \cdot 10^{-2} \frac{g}{cm^3}$ and the dynamical viscosity to $\nu = 3.3 \cdot 10^{-2} \frac{cm^2}{s}$. As for the space discretization, $\mathbb{P}_1 - \mathbb{P}_1$ finite elements are chosen while for for the time discretization an order 2 BDF scheme is selected with order 2 Newton-Gregory extrapolation. Boundary conditions are assigned as described in section 2.3, in particular the flow-rate used in the definition of the INLET boundary condition is the one depicted in figure (6).

Running the simulations on clusters shows that the computational cost using the VMS-LES stabilization is excessively high, therefore we opted for the SUPG stabilization. For instance, table 1 shows a comparison between the two stabilizations in the cases of a serial and two parallel runs on two and four processors. It can be seen that in the serial case VMS-LES takes more than 5 times the time of SUPG. In the parallel cases this ratio reduces, however the speed-up between 2 and 4 processors is sensibly smaller than the one between one and two. Moreover, while for SUPG assembling the stabilization term takes less than a half of the execution time, for VMS-LES this ratio grows to about 90% (in both serial and parallel cases). To conclude, assembling of the VMS-LES stabilization term is the bottleneck of the execution and its high computational cost does not allow to justify the use of this technique in simulations.

Table 1: Comparison between SUPG and VMS-LES

Stabilization	# processors	Time assembly (s)	Total time (s)	% time assembly over total time
SUPG	1	10.06	22.89	44.0
VMS-LES	1	111.75	125.0	90.0
SUPG	2	8.26	18.11	45.6
VMS-LES	2	75.39	84.99	88.7
SUPG	4	6.83	13.09	52.14
VMS-LES	4	68.46	73.56	93.1

Mean execution times of one timestep of the finite-elements solver. The mesh is a coarsened version of the mesh used in actual simulations. Values reported in the table are an average taken over 10 consecutive timesteps. Values are obtained from execution on a workstation, therefore the number of processors is limited to 4.

The timestep employed for the pre-operational simulation is $\Delta t = 0.001s$ and solutions are exported every 5 time-steps (as well as the previous time-step to allow the simulation to be restarted, as described in section 5) for two heart-beats. Using the same time-step for the post-operational case leads to the formation of spurious modes for pressure(see figure 7b) from time 0.34s (during the first heart-beat) on. However, reducing the time-step by a half ($\Delta t = 0.0005$s) results in a solution in which the pressure field is not affected by spurious modes. In this case the simulation is run for a time equal to four heart-beats. In both pre and post operational simulation it can be seen that values at the beginning and end of the last heart-beat are extremely close, implying that the initial transient dynamics caused by the choice of the initial condition has vanished.

In this section results of pre and post-operational simulations are presented, in particular for each of them a qualitative description of the blood flow is given and results regarding the quantities of interest (WSS, OSI, TAWSS, ECAP, pressure drops) are described. Finally, results are compared to highlight differences in their main features. As the aim of the project is to study the effect of the EVAS on the neck of the aneurysm, the results here presented concern only this part of the computational domain, both in the pre and post-operational simulations.

As for the description of time-dependent quantities (the blood flow, WSS and pressure drops) the following nomenclature will be used to refer to time intervals (see figure 7):

- Early systole, $t \in (0.075, 0.175)s$: the time interval between when the flow-rate is close to zero and the systolic peak. In this period the heart starts pumping blood in the vascular system, therefore the flow-rate is increasing;

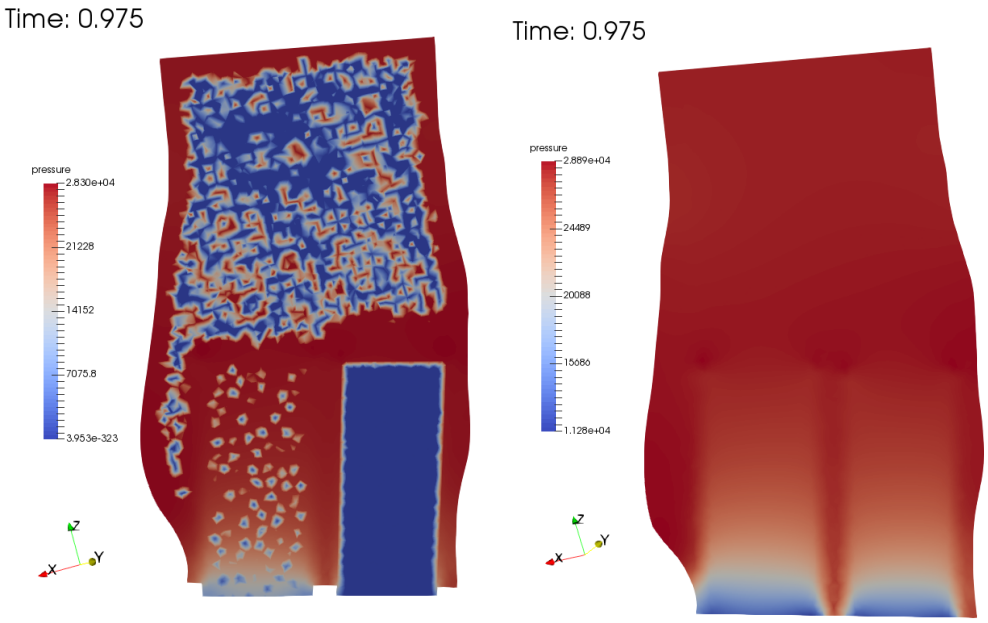

(a) (b)

Figure 7: (a): Solution of the post-operational problem with SUPG at time 0.175s with timestep $\Delta t = 0.001s$ of the second heart-beat. The pressure field is visualized in the region of the neck. Spurious modes for pressure are clearly visible; (b) solution at the same time for SUPG with timestep $\Delta t = 0.0005s$

- Late systole, $t \in (0.175, 0.345)s$: between the systolic peak and the time when flow-rate reaches zero again (i.e. approximately when the heart stops pumping blood);
- Early diastole, $t \in (0.345, 0.500)s$: between the following two instants when the flow-rate is zero. In this interval the flow-rate is negative, therefore back-flows are present;
- Late diastole, $t \in (0.500, 0.800)s$: the following part of diastole. In this long interval the flow-rate oscillates above and below zero with a small amplitude (if compared to the systolic peak).

6.1 Pre-operational simulation

During early systole the blood flow evolves from a state of relative stagnation, where there is no dominant direction for the velocity field, to an almost unidirectional flow when the highest velocities magnitudes of the simulation are recorded (between 50 and $60\frac{cm}{s}$). During late systole, the formation and growth of recirculation regions can be noticed, especially where the vessel wall is more irregular. At the same time the portion of domain where the flow is unidirectional shrinks (figure 8a). During early diastole, back-flows originate both in the aneurysm lumen and in the neck, with a magnitude as high as about 30 $\frac{cm}{s}$ (in the region where the flow was before recirculating). During this interval, back-flows generate along most part of the vessel wall (see figure 8b). Once the flow-rate has past its negative peak (time $t = 0.405s$) and is approaching zero again, back-flows become fainter and in general the magnitude of the velocity field decreases and starts to stagnate. Finally, during the phase of late diastole the flow does not show any easily identifiable pattern. During this period the velocity field has small magnitude, always below $10\frac{cm}{s}$, especially close to the vessel wall. As shown in figure 9a (the time average of the velocity field) the only region where a recirculating flow is present for a predominant time is the bulge above the aneurysm.

As for WSS, during early systole it tend to align toward the opposite direction of the flow with increasing magnitude (maximum of 0.35 $\frac{dyn}{cm^2}$ at systolic peak located in the lower part of the neck, where the vessel wall is more irregular) (see figure 10a and 10b). Starting from late systole until when flow-rate reaches its minimum value, WSS gradually change direction and end up pointing toward the bottom by when the

flow-rate at the inlet is zero again. During this period maximum magnitude is attained on the bulge of the neck above the aneurysm, while the other side of the neck presents an area in the upper section where WSS has lower magnitude (see figure 10c and 10d). After this, when the flowrate is returning zero, magnitude of WSS gradually decreases everywhere without changing direction. During the last period of diastole WSS have small magnitudes compared to the previous part of the heart-beat with varying directions.

The time evolution of WSS is summarized by its time-average TAWSS. Among its features, it can be seen that its maximum is attained in the region of the neck between the aneurysm and the bulge located just above (see figures 11a). Also note that there are regions around the bulge and on the other side of the neck where TAWSS has small values (11a and 11b).

As for OSI, peak values are recorded around the same bulge, but also on the other side of the neck, where WSS were usually less intense but more variable in direction (see figures 11c and 11d).

Looking at ECAP, which should be regarded as the most significant index under the medical point of view, part of the latter mentioned region also experiences high ECAP values, as well as another region close to the bulge above the aneurysm. (see figures from 12a to12d). The definition of ECAP as ratio of OSI and TAWSS is clearly visible, as high values of ECAP are located where OSI is big and TAWSS is small.

Finally pressure drops between inlet and outlet as a function of time is shown in figure 13.

6.2 Post-operational simulation

At the beginning of the early systolic phase the flow has a moderate velocity. No principal direction is present in the upper part of the neck, while the lower part displays a vorticous region between the tubes of the EVAS and the vessel wall. During this phase, as in the pre-operational case, the flow becomes almost unidirectional in the upper part of the neck, but in the lower part the flow is parallel to the sealing and attains here its maximum velocity close to the tubes(see figure 8c). During late systole the dynamics of the flow is analogous to the one of the pre-operational case, with growing regions of recirculation close to the vessel wall and in the region above the sealing.

During early diastole, when the flow-rate is negative in the inlet, the recirculation region above the sealing grows and the formation of back-flows can be seen both in the stents and in the neck (figure 8d). After the flow-rate has attained its minimum an is returning to zero in can be seen that the back-flows decrease in intensity. Still, the recirculation above the sealing is present. This recirculation persists during late diastole, while in the rest of the domain the flow has small magnitude and no preferential direction. As shown in figure 9b (the time average of the velocity field) the only region where a recirculating flow is present for a predominant time is the one above the sealing far from the stents.

As for WSS, during early systole it aligns with the opposite direction of the flow, as in the pre-operational case. However, in this case maximum values are attained in the narrow region between the tubes and the vessel wall (figure 10e). These values are considered an artifact of the simulation caused by the fact that in these regions the mesh is not fine enough to describe the physical flow. During late systole and early diastole WSS tends to change direction everywhere with a more complex patter than in the operational case (figures 10g and10h).

As for TAWSS, peak values can be observed close to the narrow gaps between the tubes and the neck. These values are treated as artifacts of the simulation, as explained above. However, other relatively high values are present on the bulge (see figure 11e). Low values of TAWSS are present on most of the other side of the neck (figure 11f).

As for OSI, high values are located on the side of the bulge (figure 11g) and on the other side of the neck (figure 11h) as in the pre-operational problem, but also on a region close to the sealing (on the left of the same figure).

As for ECAP, several small artifact are present close to the sealing surface and between one of the tubes and the neck (figure 12g12h), with values of the order of 10^3. Relevant high values of ECAP (about 200 $\frac{dyn}{cm^2} \cdot s$) are recorded in a region close to the sealing (figure 12f). Other relevant regions are shown in figures 12e and 12g.

Finally, the difference of pressure between inlet and outlet is shown in figure 13.

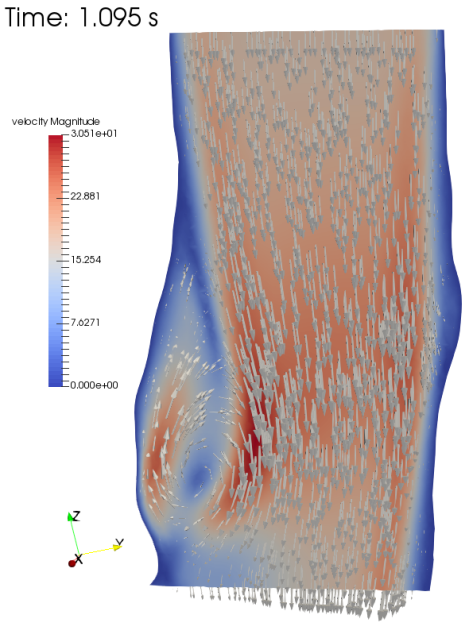

(a) Section of the pre-operational solution at time 0.295s of the second heart-beat.

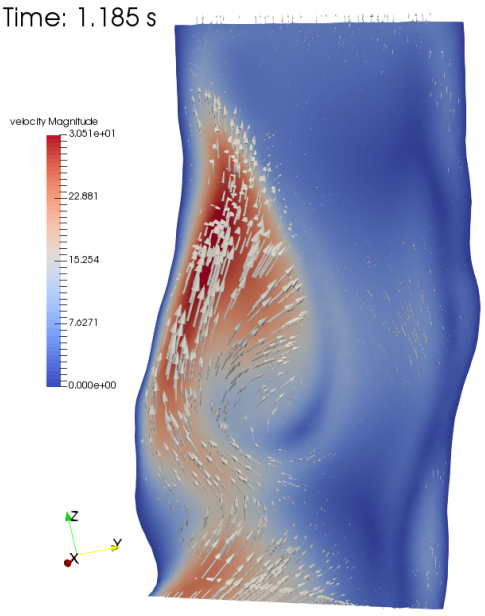

(b) Section of the pre-operational solution at time 0.385s of the second heart-beat.

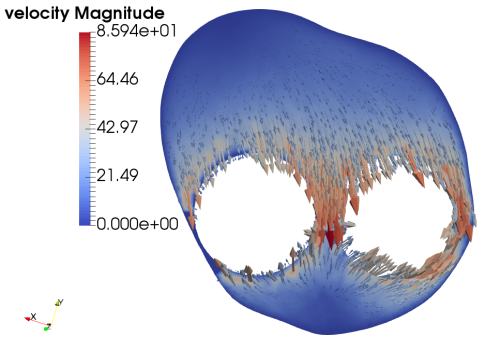

(c) Section of the post operational solution parallel and close to the sealing's top surface at time 0.15s of the third heart-beat.

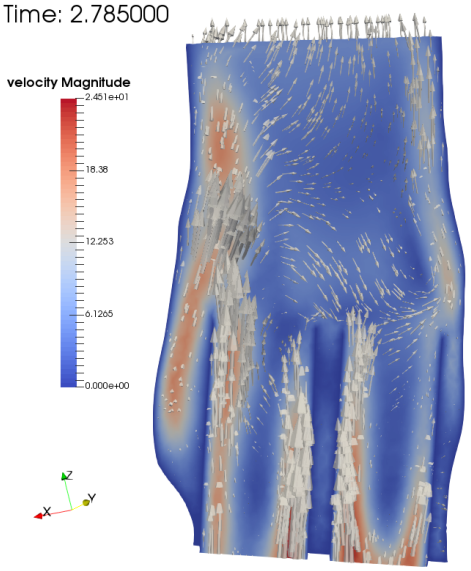

(d) Section of the post operational solution at time 0.385s of the third heart-beat.

Figure 8: Some representations of the solutions of pre (first row) and post operational problems(second row). All sections are colored with the velocity field magnitude ($\frac{cm}{s}$), arrows indicate its direction.

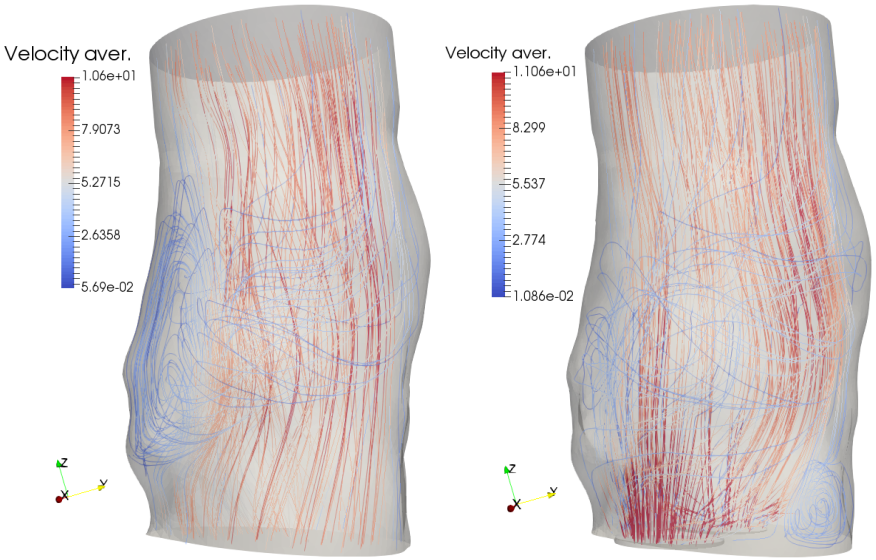

(a) (b)

Figure 9: Time average over a heart-beat of the velocity field for the pre operational (left) and post-operational solution (right)

6.3 Comparison of the results

The flows in pre and post operational conditions display different dynamics, reflected in the difference of their time-averages (figure 9). Among the differences, we highlight the presence of recirculation regions located in different regions: in the bulk above the aneurysm for the pre-operational case and just above the sealing surface for the post-operational one.

Differences in WSS between the two simulations are reflected by their time average shown in the left part of figure 11. Apart from the artifacts located close to the stents, it can be seen that WSS tend to assume, on average not as high but comparable values to the per-operational case.

Differences between values of OSI between pre and post-operational solutions can be seen in the right part of figure 11. Among the main differences are the different values around the bulge above the aneurysm, higher in the pre-operational case.

As for ECAP, differences are also present. Comparing figures 12a and 12e, a region of high values of ECAP appear in the bottom left part of the post operational solution, while the one on the top right of the pre operational case disappear. This is probably caused by the presence of the stents, which leads to the formation of a narrow gap when the flow slows down (thus high TAWSS) and is less coherent over time (this high OSI). Comparing figures 12b with 12f (and 12c with 12g)the second main difference can be seen: the post operational solution displays a region at the bottom (the one in which the highest values of ECAP are recorded) that is not present in the pre-operational case. These values are attributed to the presence of the sealing and of the stents, which cause the flow to slow down and change direction over time.

Finally, pressure differences between inlet and outlet are much higher for the post-operational case than the pre operational one (see figure 13). This difference can be attribute to the presence of the sealing and the stents, which reduce the surface through which blood can flow. However, when reading these results, it must be remembered that in this simulation boundaries (the vessel wall, the interface with the sealing and the stents) are considered as rigid (see next section).

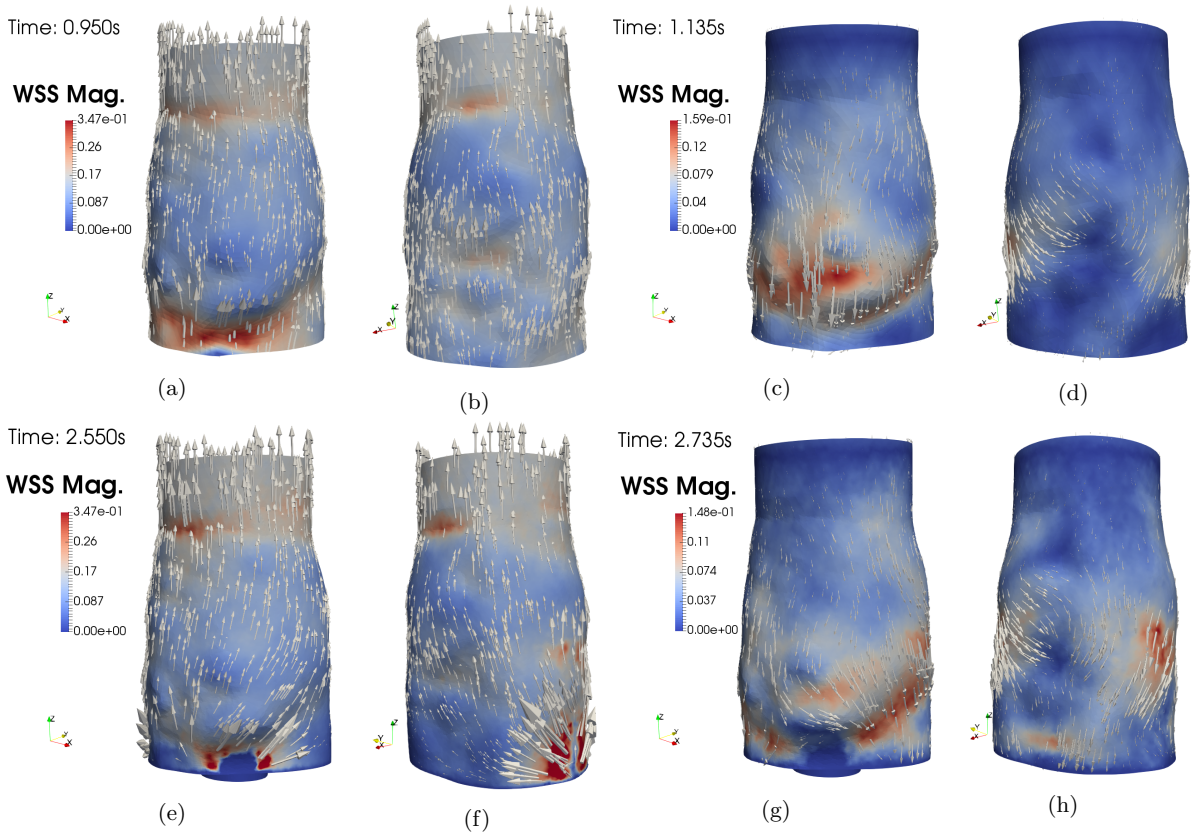

Figure 10: Comparison between WSS for pre (first row) and post operational (second row) solutions. The first two pictures of each row are WSS at time 0.150s during respectively the second and the fourth heart-beat, the last two for time 0.335s respectively during the same heart-beats.

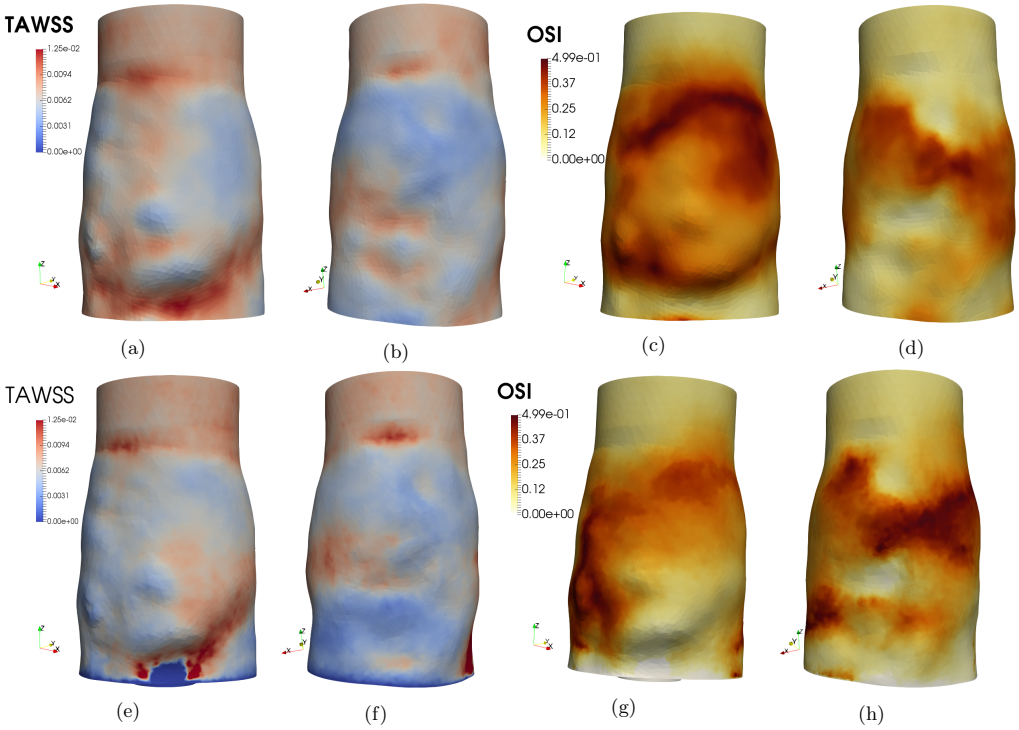

Figure 11: Comparison of TAWSS (first two columns) and OSI (last two columns) between pre operational (first row) and post operational (second row)problems. Two perspectives (obtained one from the other rotating the domain of 180° degrees)for each are shown.

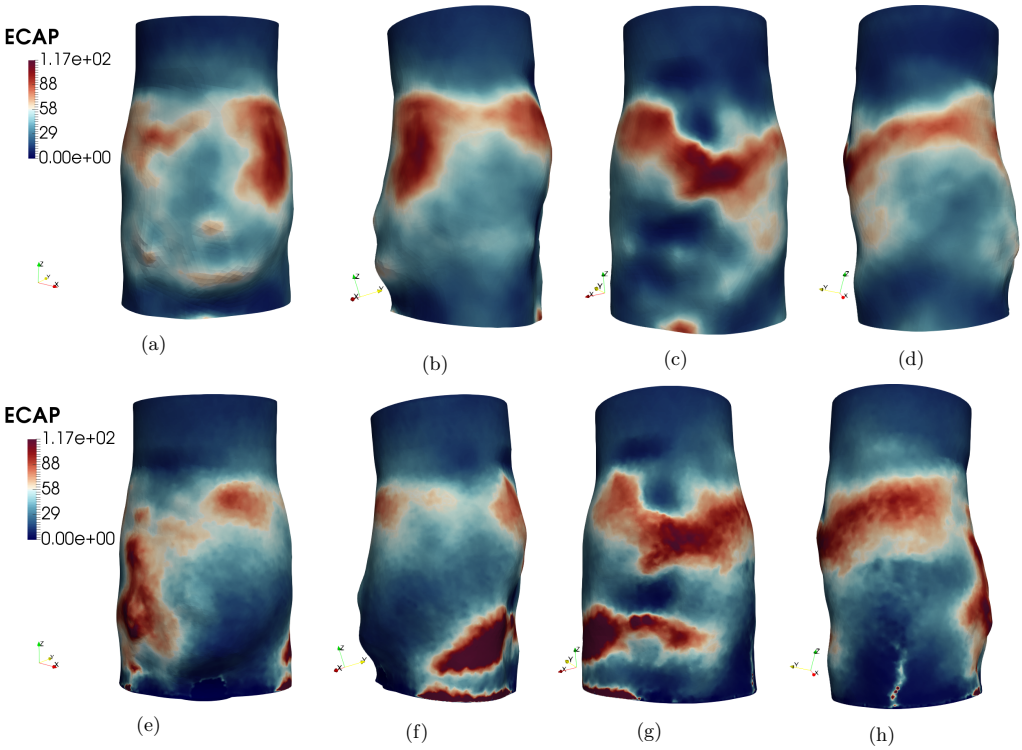

Figure 12: Comparison of ECAP from pre operational (first row) and post-operational (second row) solutions. Four perspectives (obtained one from the other rotating the domain by 90°) for each are shown.

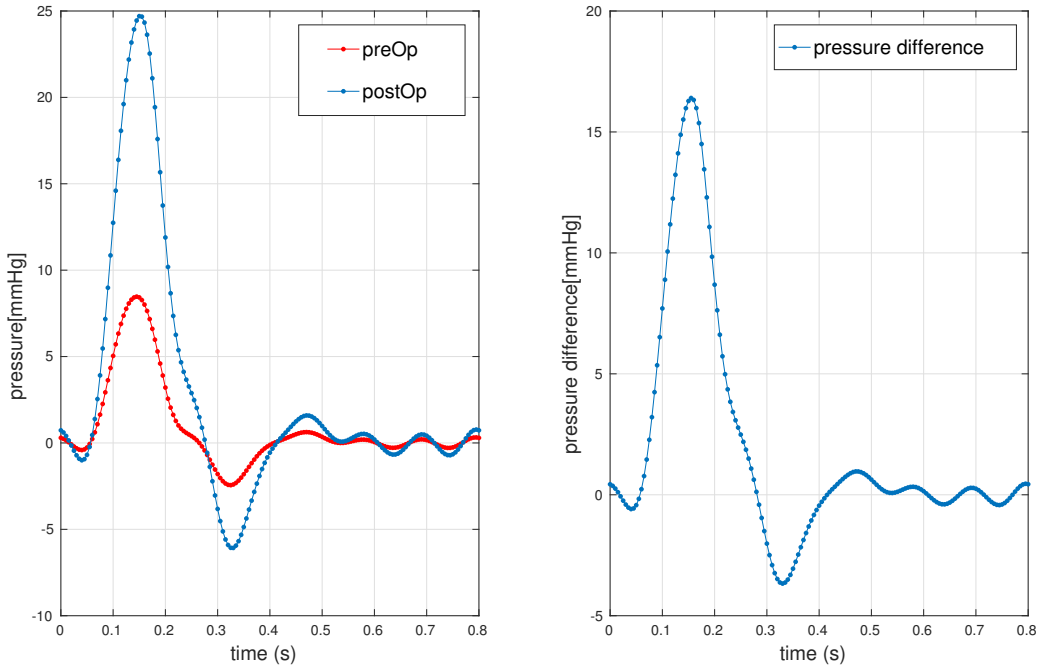

Figure 13: On the left, pressures from the pre operational (red) and post operational (blue) solutions as a function of time recorded during one heart-beat. On the right their difference.

7 Conclusions and on-going work

During the project presented in this report numerical simulation for the blood flow in an AAA and after EVAS are set up and run. Results are physically sound (within the limits of the the model chosen to describe the problems) expect for some numerical artifacts, which however can be easily detected. Numerical results allowed to compare the pre and post operational blood flow, leading to the conclusion that the two present some radically different features, such as the presence of regions of recirculation located in different position. In particular ECAP, an index used to detect regions of blood vessels with high risk of formation of intraluminal thrombi, is used to draw some conclusions on the potential negative effect of the surgical device on the aneurysm's neck, the section of abdominal aorta located above the aneurysm and below the renal arteries. The analysis of this index lead to the conclusion that regions at high risk of formation of thrombi are not the same before and after the device is placed. In particular new regions with high values of ECAP are present in the region just above the sealing and in the narrow gap between the stents and the neck (see figure 12). Another important result comes from the comparison between pre and post-operational results of pressure drops between inlet and outlet. It can be seen that the post operational blood flow presents higher pressure drops, with a difference above 15 mmHg.

The work presented in this report can be improved and extended in a number of different ways. A possible future development is the use of fluid-structure interaction models rather than a simple fluid flow simulation. This would allow to take into account the compliance of the vessel wall rather than considering it rigid. As a matter of facts, there is a strong coupling between the blood flow and the vessel deformation. An example is the *Windkessel effect*, which consists in the deformation of the artery, therefore accumulation of elastic energy, during systole. Then, during diastole, this energy is released resulting in a smoothening of the pulsatile flow. This phenomenon also tends to decrease pressure drops between inlet and outlet of the domain, which is the reason why the results on pressure drops obtained in this project are considered a higher estimate of the real values.

Another possible development is the extension of the computational domain. On one side, the domain

could be extended above to include the upper section of the abdominal aorta and the renal arteries. Investigating the blood flow in this region is important because it is believed that the presence of the EVAS device causes backflows to alter the blood flow in the renal arteries. However, it must be remarked that the main obstacle of this development is the current lack of suitable segmentation techniques to isolate the renal arteries from medical images. Therefore, a preliminary and necessary step would be to extend currently used segmentation algorithms. On the other side, the domain can be extended below to include the region of iliac arteries where the stents of the EVAS device end. This extension is motivated by the fact that a possibly pathogenic blood flow could be present in these regions. Just as in the aneurysm neck (in the post-operational case), localizing regions with high values of ECAP may allow to draw some conclusions on the post-operational flow in these regions.

Another possible improvement on the results could come from the use of a locally refined mesh. The choice of a suitably refined mesh could allow to better approximate the physical flow in some regions, for example in the narrow gap between the neck and one of the stents, where the use of only one layer of element causes the flow to be identically zero in that region, a non-physical approximation. Moreover, the mesh could be coarsened in other regions where a precise description of the flow is not of central importance, resulting in a possibly lower computational cost of the simulation.

Finally, the use the VMS-LES stabilization may be desirable. To achieve this, a strategy to reduce its computational cost is needed. An option could be to employ a different computational mesh as mentioned above.

References

[1] Sakalihasan, N., Limet, R. and Defawe, O.D., 2005. Abdominal aortic aneurysm. The Lancet, 365(9470), pp.1577-1589.

[2] de Bruin, J.L., Brownrigg, J.R., Karthikesalingam, A., Patterson, B.O., Holt, P.J., Hinchliffe, R.J., Morgan, R.A., Loftus, I.M. and Thompson, M.M., 2015. Endovascular aneurysm sealing for the treatment of ruptured abdominal aortic aneurysms. Journal of Endovascular Therapy, p.1526602815582529.

[3] Roy, D., Kauffmann, C., Delorme, S., Lerouge, S., Cloutier, G. and Soulez, G., 2012. A literature review of the numerical analysis of abdominal aortic aneurysms treated with endovascular stent grafts. *Computational and mathematical methods in medicine, 2012*.

[4] Di Achille, P., Tellides, G., Figueroa, C.A. and Humphrey, J.D., 2014, December. A haemodynamic predictor of intraluminal thrombus formation in abdominal aortic aneurysms. In *Proc. R. Soc. A* (Vol. 470, No. 2172, p. 20140163). The Royal Society.

[5] Les, A.S., Yeung, J.J., Schultz, G.M., Herfkens, R.J., Dalman, R.L. and Taylor, C.A., 2010. Supraceliac and infrarenal aortic flow in patients with abdominal aortic aneurysms: mean flows, waveforms, and allometric scaling relationships. *Cardiovascular engineering and technology*, 1(1), pp.39-51.

[6] Nichols, W., O'Rourke, M. and Vlachopoulos, C. eds., 2011. *McDonald's blood flow in arteries: theoretical, experimental and clinical principles*. CRC press.

[7] Quarteroni, A., 2010. *Numerical models for differential problems (Vol. 2)*. Springer Science & Business Media.

[8] Forti, D. and Dedè, L., 2015. Semi-implicit BDF time discretization of the Navier–Stokes equations with VMS-LES modeling in a High Performance Computing framework. *Computers & Fluids*, 117, pp.168-182

[9] Brooks, A.N. and Hughes, T.J., 1982. Streamline upwind/Petrov-Galerkin formulations for convection dominated flows with particular emphasis on the incompressible Navier-Stokes equations. Computer methods in applied mechanics and engineering, 32(1-3), pp.199-259.